ADVANCED ELECTRONIC MATERIALS
www.advelectronicmat.de

# Tunable Two-Channel Magnetotransport in $SrRuO_3$ Ultrathin Films Achieved by Controlling the Kinetics of Heterostructure Deposition

*Eun Kyo Ko, Han Gyeol Lee, Sangmin Lee, Junsik Mun, Jinkwon Kim, Ji Hye Lee, Tae Heon Kim, Jin-Seok Chung, Suk Bum Chung, Sang Hwa Park, Sang Mo Yang, Miyoung Kim, Seo Hyoung Chang,* and Tae Won Noh**

**In the field of oxide heterostructure engineering, there are extensive efforts to couple the various functionalities of each material. The Berry curvature-driven magnetotransport of $SrRuO_3$ ultrathin films is currently receiving a great deal of attention because it is extremely sensitive to the electronic structures near the Fermi surface driven by extensive physical parameters such as spin–orbit coupling and inversion symmetry breaking. Although this is beneficial in terms of heterostructure engineering, it renders transport behavior vulnerable to nanoscale inhomogeneity, resulting in artifacts called "hump anomalies." Here, a method to tune the magnetotransport properties of $SrRuO_3$ ultrathin films capped by $LaAlO_3$ layers is developed. The kinetic process of pulsed laser deposition by varying the growth pressure during $LaAlO_3$ layer deposition is systematically controlled. Furthermore, the effects of nanoscale inhomogeneity on the Berry curvature near the Fermi surface in $SrRuO_3$ films are investigated. It is found that the high kinetic energy of the capping layer adatoms induces stoichiometric modification and nanoscale lattice deformation of the underlying $SrRuO_3$ layer. The control of kinetics provides a way to modulate magnetization and the associated magnetotransport of the $SrRuO_3$ layer.**

## 1. Introduction

Heterostructural engineering of perovskite oxides has been widely studied due to its physical implications and practical applications.[1–3] Perovskite oxides ($ABO_3$) are suitable building blocks for oxide electronics. The physical properties can be extensively modulated by varying the A- and B-site ions while maintaining structural similarity. At the heterointerface, interfacial coupling between charge, lattice, and spin induces intriguing emergent phenomena, including 2D conduction,[1,4] ferroelectricity,[5] magnetism,[6] and superconductivity.[7]

Perovskite $SrRuO_3$ (SRO) is one of the most extensively studied oxides by heterostructural approach.[8] Bulk SRO has a metallic and ferromagnetic ground state with a Curie temperature ($T_C$) of ≈160 K.[9]

E. K. Ko, H. G. Lee, J. Kim, J. Lee, T. W. Noh
Center for Correlated Electron Systems
Institute for Basic Science (IBS)
Seoul 08826, Republic of Korea
E-mail: twnoh@snu.ac.kr

E. K. Ko, H. G. Lee, J. Kim, J. Lee, T. W. Noh
Department of Physics and Astronomy
Seoul National University
Seoul 08826, Republic of Korea

S. Lee, J. Mun, M. Kim
Department of Materials Science and Engineering and
Research Institute of Advanced Materials
Seoul National University
Seoul 08826, Republic of Korea

T. H. Kim
Department of Physics and Energy Harvest-Storage
Research Center (EHSRC)
University of Ulsan
Ulsan 44610, Republic of Korea

The ORCID identification number(s) for the author(s) of this article can be found under https://doi.org/10.1002/aelm.202100804.

**DOI: 10.1002/aelm.202100804**

J.-S. Chung
Department of Physics
Soongsil University
Seoul 06978, Republic of Korea

S. B. Chung
Department of Physics
University of Seoul
Seoul 02504, Republic of Korea

S. B. Chung
Natural Science Research Institute
University of Seoul
Seoul 02504, Republic of Korea

S. B. Chung
School of Physics
Korea Institute for Advanced Study
Seoul 02455, Republic of Korea

S. H. Park, S. M. Yang
Department of Physics
Sogang University
Seoul 04107, South Korea

S. H. Chang
Department of Physics
Chung-Ang University
Seoul 06974, Republic of Korea
E-mail: cshyoung@gmail.com

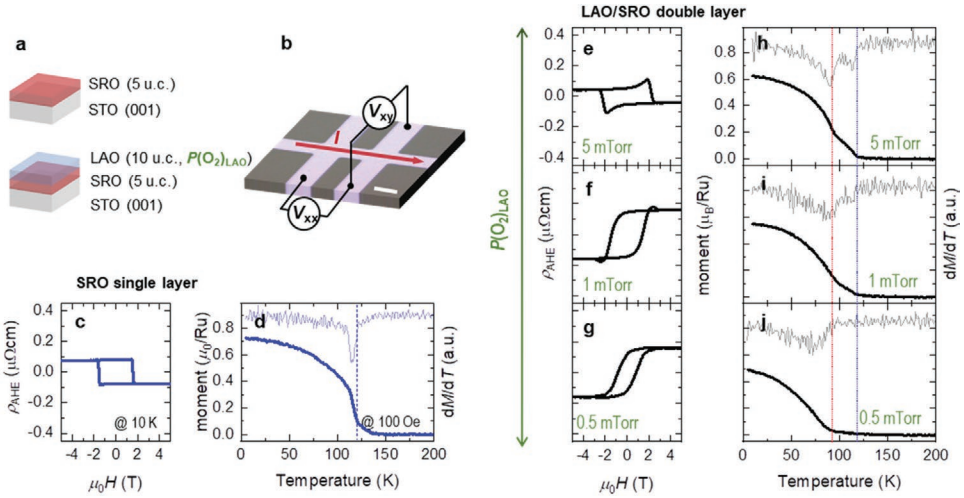


**Figure 1.** Field-dependent anomalous Hall resistivity ($\rho_{AHE}$–$H$) curves and temperature-dependent magnetization ($M$–$T$) curves of $SrRuO_3$ (SRO) and $LaAlO_3$ (LAO)-capped SRO films. a) 5 u.c. SRO films and with and without the capping layers. b) Optical microscopic image of 50 × 50 μc$^2$ Hall bar. The scale bar indicates 50 μm. c) $\rho_{AHE}$–$H$ curves of 5 u.c. SRO films without capping layers measured at 10 K. All linear terms from the ordinary Hall effect have been subtracted. d) $M$–$T$ curves of 5 u.c. SRO films without capping layers. The black solid lines are the experimental data and the gray solid lines are the first derivative curves. e–g) $\rho_{AHE}$–$H$ curves of LAO-capped SRO films. The growth conditions and thicknesses of the SRO layers were fixed while the oxygen pressure during LAO layer growth [$P(O_2)_{LAO}$] was varied from 5 to 0.5 mTorr. h–j) $M$–$T$ curves of LAO-capped SRO films. The blue (red) dotted lines were derived at Curie temperatures ($T_C$) of ≈120 K (≈90 K).

Given the large conductivity ($10^4\ \Omega^{-1}\ cm^{-1}$) at room temperature, SRO films have been widely used for decades as the electrodes of all-oxide heterostructures.[10] It has anomalous Hall transport properties below $T_C$; SRO can thus be used for spintronic applications.[8,11] Recent magnetotransport studies of SRO ultrathin films have opened a new avenue in the search for topological phenomena in oxide heterostructures. For example, real-space topological object (magnetic Skyrmion) has been found in $SrIrO_3$/SRO.[12,13] Besides, momentum-space topological phenomena [anomalous Hall effect (AHE)] have been described in ultrathin SRO films.[14] The key features of AHEs are governed by the sum of the Berry curvature along the Fermi surface. A subtle balance among broken time-reversal symmetry, a strong correlation, and spin–orbit coupling generate non-trivial band-crossing points and finite Berry curvatures.[14–16] Therefore, the intriguing topological properties of SRO ultrathin films can be tuned by carefully controlling the band structures, which are highly sensitive to external parameters.[17–26]

However, the high sensitivity of SRO to external parameters has also given rise to significant concerns about inhomogeneity-induced artifacts in the AHEs.[27–36] If significant inhomogeneities are present, spatial regions that are magnetized differently contribute to the AHE signal. Particularly, if two types of region with opposite AHE signs are present, the field-dependent Hall signal can mimic the "hump anomaly," similar to that of the topological Hall effect (THE).[12,13,37,38] Such a two-channel AHE can be induced by inhomogeneous film thickness,[30,31] structural variation,[32] Ru vacancies,[33] and interfacial effects.[34,35] More recently, the ion irradiation has been used for post-synthesis control of AHE.[36]

Here, we systematically control the inhomogeneity of SRO ultrathin films by depositing the $LaAlO_3$ (LAO) capping layer in situ. We grew several SRO films under identical conditions using pulsed laser deposition (PLD). We then deposited LAO layers under different oxygen pressures and manipulated the deposition kinetics. As an LAO has a light cation, it generates a highly kinetic plume at low oxygen pressure during PLD. After LAO deposition, we investigated the magnetotransport properties of the LAO/SRO double layer. As LAO is a simple band insulator, the transport properties of an LAO/SRO heterostructure will be determined only by the conducting SRO layer. Strikingly, even when the growth conditions and thicknesses of the SRO layers were precisely fixed, simple variation of the LAO growth pressure triggered significant changes in the AHE signals and hump anomaly. Nanoscale compositional analysis revealed that the stoichiometry of the underlying SRO layer was disturbed during LAO layer deposition. We found that the resulting distribution of inhomogeneous magnetization served as a tuning knob allowing in situ control of the two-channel AHEs of SRO films.

## 2. Results and Discussions

We grew SRO single-layer and LAO/SRO double-layer films on $SrTiO_3$(001; STO) substrates using the PLD technique (**Figure 1**a, see the Experimental Section for details). The thickness of SRO ultrathin films was five-unit cell (u.c.). We precisely monitored the thickness variation during the growth with the reflection high-energy electron diffraction patterns (Figure S1, Supporting Information) to avoid artifacts from the thickness inhomogeneity.[30,31] We also grew LAO/SRO double-layer films by depositing 10-u.c.-LAO capping layers. The growth conditions were identical for all SRO layers, but we systematically varied the growth pressure during LAO layer deposition. To confirm film quality, we checked the topography by using atomic force microscopy (AFM) and X-ray diffraction (XRD). All samples had atomically flat surfaces and high crystallinity,

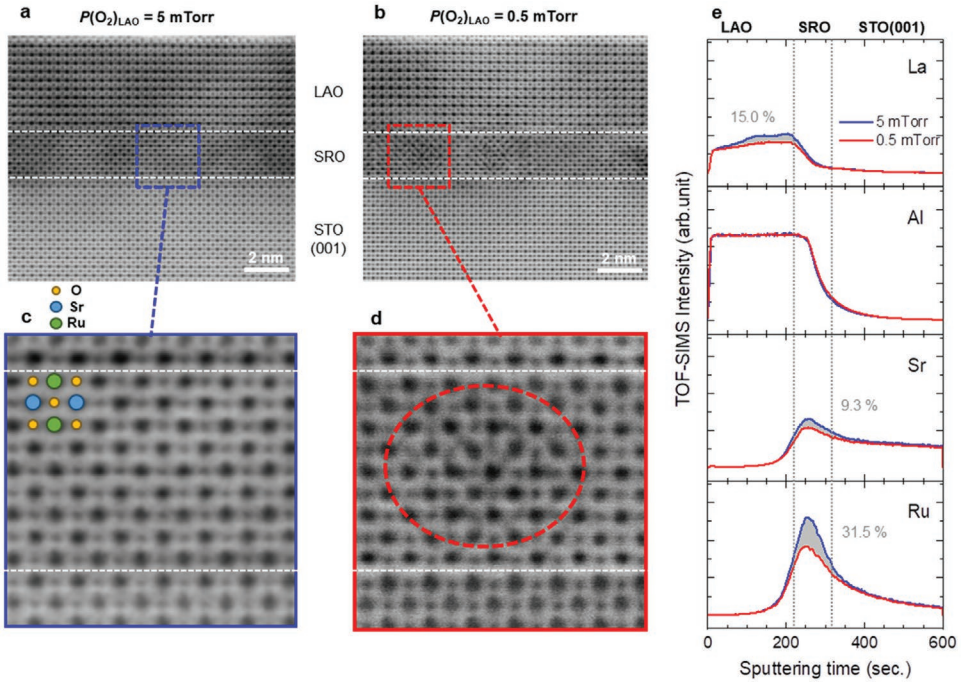


**Figure 2.** Scanning transmission electron microscopy (STEM) images, obtained in annular bright-field (ABF) mode, of LAO-capped SRO films, and their time-of-flight secondary ion mass spectra (TOF-SIMS). a,b) STEM images of LAO-capped SRO when $P(O_2)_{LAO}$ = 5 and 0.5 mTorr, respectively. c) Enlarged image of the blue dashed square in (a). d) Enlarged images of the red dashed square in (b). The atomic positions of cations and oxygens are well-defined in the $P(O_2)_{LAO}$ = 5 mTorr sample, but not in the $P(O_2)_{LAO}$ = 0.5 mTorr sample. The elongation and uncertainty of positioning is highlighted in red dashes. e) Depth profile of the TOF-SIMS. The blue solid line is that from the $P(O_2)_{LAO}$ = 5 mTorr sample and the red solid line indicates the $P(O_2)_{LAO}$ = 0.5 mTorr sample. The gray areas indicate differences between the samples. The gray digits indicate the proportions of grey areas, as revealed by the integrated TOF spectra from the 5-mTorr sample. Ru deficiency is mainly observed in the SRO layer.

regardless of whether an LAO capping layer was present (Figures S2 and S3, Supporting Information).

We measured the magnetotransport and magnetic properties of SRO single-layer films. We prepared a 50 × 50 μm$^2$ Hall bar and used it to obtain field-dependent transverse resistivity ($\rho$–$H$) (Figure 1b). By subtracting the linear term (ordinary Hall effect) from the $\rho$–$H$ curves, we derived AHE curves ($\rho_{AHE}$–$H$, see Figure S4, Supporting Information). In SRO, it is known that the AHE is generated by the Berry curvature.[15] Recent works have shown that an AHE sign change can occur between 4 and 5 u.c.[21,23,30,31] Our SRO films exhibited negative AHEs in the $\rho_{AHE}$–$H$ curves (Figure 1c), as expected for a 5-u.c. film. There was no hump anomaly; such humps are commonly observed in SRO films of inhomogeneous (fractional) thickness,[30,31] indicating that our SRO film has integer thickness. Figure 1d shows the magnetization–temperature ($M$–$T$) curves, measured using a 100-Oe out-of-plane magnetic field. $M$ began to increase significantly around 120 K. To better understand the effect, we derived the first derivatives of the $M$–$T$ curve (the fine solid line). A sharp drop was apparent near 120 K; this was the Curie temperature ($T_C$).

Intriguingly, we found that the AHEs of LAO/SRO double-layer films were greatly affected by the oxygen pressure during the growth of the top LAO insulating layer [$P(O_2)_{LAO}$]. When the layer was grown at a $P(O_2)_{LAO}$ of 5 mTorr, the capped SRO layer still exhibited a negative sign of AHE, but with a hump anomaly near the coercive field (Figure 1e). When the $P(O_2)_{LAO}$ was decreased, the sign of AHE signal flipped from negative to positive and a small hump anomaly remained (Figure 1f). With a further $P(O_2)_{LAO}$ decrease to 0.5 mTorr, the sign of AHE remained positive but the hump anomaly vanished (Figure 1g). If the hump was attributable to a Skyrmion-induced THE, the hump intensity should be controllable by manipulating the applied current.[39] However, as shown in Figure S5 (Supporting Information), the hump signal barely varied according to the applied current. In addition, the hump anomaly occurred as the AHE sign flipped. This suggests that the hump anomaly in our LAO/SRO double layers reflects a two-channel AHE rather than a THE.

To further explore the effects of $P(O_2)_{LAO}$, we measured the $M$–$T$ curves of the LAO/SRO double-layer films. In the pioneering paper of Fang et al.,[15] it was reported that an AHE of SRO depended strongly on the $M$ value. More recent theoretical works have shown that $M$ should play important roles in $\rho_{AHE}$–$H$ curves, because $M$ tunes the SRO band-crossing points, thus modifying the Berry curvature-driven AHE.[21] Figure 1h,i shows the $M$–$T$ curves and their first derivatives for the LAO/SRO double-layer films. Interestingly, for films grown at $P(O_2)_{LAO}$ values of 5 and 1 mTorr, the $M$–$T$ curves exhibit broad ferromagnetic transitions. Their derivatives show two deep structures around ≈120 and ≈90 K (Figure 1h,i), suggesting the coexistence of two types of spatial regions with different magnetic properties. When $P(O_2)_{LAO}$ becomes lower (i.e., 0.5 mTorr), the regions with the ≈120 K magnetic anomaly vanish and those with the lower $T_C$ become dominant (Figure 1j).

To obtain further understandings, we performed cross-sectional scanning transmission electron microscopy (STEM) in annular bright-field (ABF) mode. **Figure 2**a,b shows STEM-ABF

images of LAO/SRO films grown with $P(O_2)_{LAO}$ = 5 and 0.5 mTorr, respectively. In both samples, the atoms of the LAO layers and STO substrates are well-defined with circular atomic shapes. However, the SRO layers differ significantly. For the $P(O_2)_{LAO}$ = 5 mTorr film, the STEM-ABF image is uniform with well-defined atomic peaks (Figure 2a). However, the $P(O_2)_{LAO}$ = 0.5 mTorr film exhibits nonuniform contrast, suggesting nanoscale inhomogeneities. Enlarged images of the blue (red) dashed square in Figure 2a (2b) are shown in Figure 2c (2d). When LAO was deposited at higher oxygen pressure, the SRO layer was relatively uniform in structure, with little deformation (Figure 2c). On the other hand, when LAO was deposited at lower pressure, the SRO atomic peaks had irregular patterns (marked by the red dashed circle). In some regions, the cation or oxygen peaks became elongated, indicating structural deformations (Figure 2d; Figure S6, Supporting Information). The SRO layer was extensively deformed when the LAO capping layer was grown at lower oxygen pressure. The spatial distribution of the inhomogeneous conductance was measured by conductive-AFM (cAFM) (Figure S7, Supporting Information).

We next performed depth-profile measurements using time-of-flight secondary ion mass spectrometry (TOF-SIMS). The LAO/SRO samples were etched with Cs (from the top) during cation mass analysis. We obtained stoichiometric depth profiles and compared the TOF-SIMS data of LAO-capped SRO samples created at $P(O_2)_{LAO}$ values of 5 and 0.5 mTorr (Figure 2e). To compare the depth profile stoichiometry of the two samples quantitatively, the intensity was normalized to that of STO(001) substrates (sputtering time from 320 s). During the initial sputtering time (0–250 s), signals from the LAO capping layer only were observed. The TOF spectra of La differed by 15.0%; those of Al did not exhibit any difference. This is consistent with an earlier report that the La/Al ratio is proportional to the PLD growth pressure up to 10 mTorr.[40] After sputtering for 250 s, atoms of the SRO layer began to contribute to the TOF spectra. Compared to the LAO layer, the stoichiometric modification was much more severe in the SRO layer. The difference was 9.3% for the Sr spectra and 31.5% for the Ru spectra, indicating many Ru deficiencies in the SRO film when a low $P(O_2)_{LAO}$ was used. Note that Ru deficiencies in SRO degrade itinerant ferromagnetism,[33,41,42] causing AHE sign reversal.[21] We found that Ru deficiencies introduced during LAO layer formation caused nanoscale structural deformations of the SRO layer, decreased $T_C$, and rendered $\rho_{AHE}$ positive. Such stoichiometric changes and structural deformations explain the coexistence of SRO nanoregions with different magnetic properties, as suggested by Figure 1h,i.

We found that the $M$–$T$ curves of all of the LAO/SRO films could be explained using a simple two-component model. The $M$–$T$ curves of LAO/SRO films grown with $P(O_2)_{LAO}$ = 50 and 0.5 mTorr exhibited simple monotonical decreases of $M$ with $T$, and apparent $T_C$ values around 120 and 90 K, respectively (**Figure 3**a,e). For convenience, we term these the 120 and 90 K phases. If the fitting is done under the assumption that all films are composed of these two phases, we can explain the $M$–$T$ curves of all LAO/SRO films (Figure 3a–e). The red and blue lines indicate the contributions from the 90 and 120 K phases, respectively. The green lines show the sums of these two contributions and agree well with the experimental data.

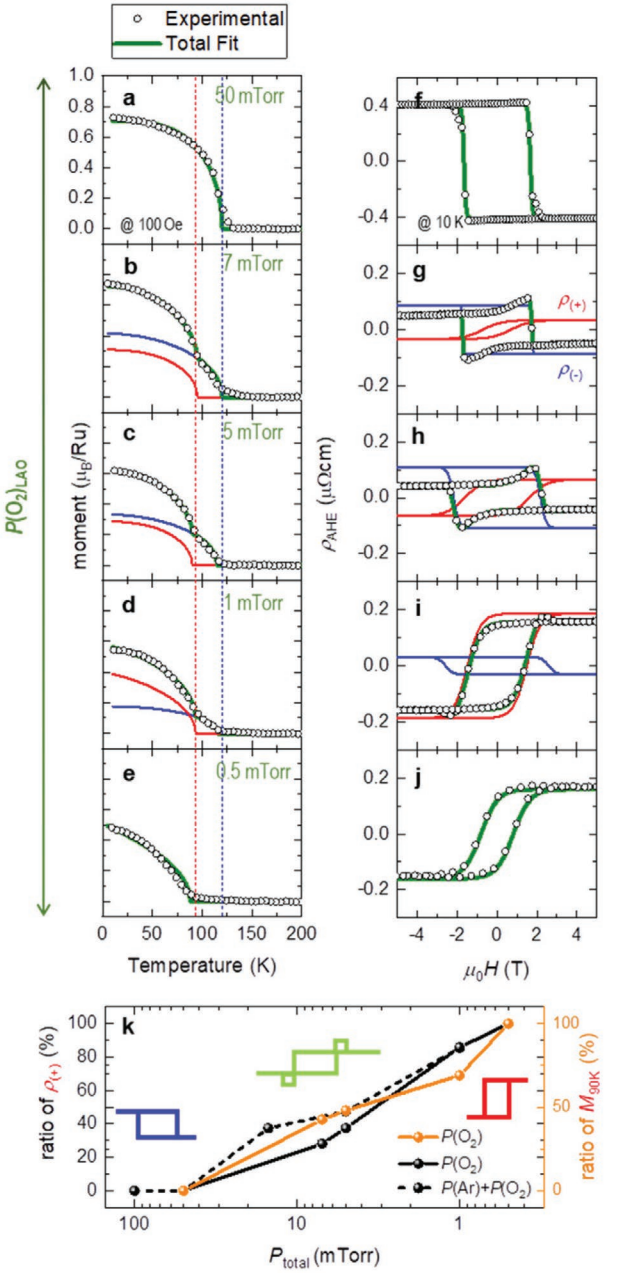


**Figure 3.** Fitted $M$–$T$ curves and $\rho_{AHE}$–$H$ values of LAO-capped SRO samples, and the ratios of the 90 K phase. a–e) Fitted $M$–$T$ curves of LAO-capped SRO samples with $P(O_2)_{LAO}$ values of 50, 7, 5, 1, and 0.5 mTorr, respectively. The red and blue curves are fitting curves at $T_C$ values of 90 and 120 K, respectively. Black open circles are experimental results and the green lines are the summations of the fitting curves. f–j) The fitted $\rho_{AHE}$–$H$ curves of LAO-capped SRO samples when the LAO layer growth pressures were 50, 7, 5, 1, and 0.5 mTorr, respectively. The red and blue curves are negative ($\rho_{(-)}$) and positive ($\rho_{(+)}$) fitting curves. k) The total pressure during capping layer growth ($P_{total}$) affects the 90 K phase ratios extracted from the fittings. The black circles are the ratios extracted from $\rho_{AHE}$–$H$ curves and the orange circles are the ratios extracted from $M$–$T$ curves. The solid lines are the results obtained when the LAO capping layers were grown under only oxygen pressure. The dashed line indicates the ratios of samples for which the LAO capping layers were grown in a mixture of argon and oxygen. As the $P(O_2)_{LAO}$ decreases, the 90 K phase ratio increases.

As shown in Figure 3k, the proportion of the 90 K phase (i.e., the Ru-deficient phase) increases as $P(O_2)_{LAO}$ decreases (see the Experimental Section for details of the fitting process).

The simple two-component model well explains the $\rho_{AHE}$–$H$ curves of all LAO/SRO films. If only the 120 K phase (90 K phase) exists, the AHE has a negative (positive) sign without any hump signal (Figure 3f,j). However, when the two phases co-exist, the AHE hump structure appears, indicating two-channel AHE (Figure 3g–i). To analyze the proportions of the two phases, we fitted $\rho_{AHE}$–$H$ curves by combining the $\rho_{AHE}$ curves with opposite AHE signs. The red and blue lines indicate the contributions of the 90 and 120 K phases to $\rho_{AHE}$, respectively. The green lines show the sum of these two phases, in good agreement with the experiments. The little variation in the magnetic coercive field might originate from nanoscale defects.[43,44] We plotted the proportions of the 90 K phase yielded by the $\rho_{AHE}$ analysis (black line in Figure 3k); these were quite consistent with those derived via $M$–$T$ analysis (the orange line). This emphasizes that it is possible to tune the magnetic and magnetotransport properties of SRO layers via in situ deposition of an LAO capping layer.

Let us discuss how we could change the physical properties of the underlying SRO films by the capping layer. As suggested by the STEM and TOF-SIMS measurements (Figure 2), the changes are closely related to the nanoscale structural and stoichiometric variations. It seemed possible that Ru might exhibit high volatility at a high LAO layer growth temperature.[45] To check this, we post-annealed SRO single-layer films for 15 min at 780 °C under an oxygen pressure of 0.5 mTorr (i.e., the lowest pressure used for LAO growth). As shown in Figure S8 (Supporting Information), post-annealing had little effect. Neither the $\rho_{AHE}$–$H$ nor $M$–$T$ curves changed significantly. Therefore, the nanoscale inhomogeneity of SRO films is not attributable to the thermodynamic instability of Ru ions at a high temperature.

The other possibility is that oxygen vacancies ($V_O$) might diffuse from the LAO layer into the underlying SRO layer.[24,46] It is known that the number of $V_O$ of LAO films can be significant if the films are grown below $10^{-6}$ Torr.[47] As we grew the LAO layers at $10^{-1}$–$10^{-3}$ Torr, it is unlikely that the layers have sufficient $V_O$ to explain the observed structural deformations. Also, at the LAO/SRO interface, the energy barrier impeding $V_O$ migration into SRO is known to be relatively high.[48,49] In addition, oxygen-deficient SRO should exhibit a large $H_C$ enhancement;[24] this was not observed in our LAO-capped SRO films. Thus, $V_O$ diffusion from the LAO to the SRO layer cannot explain the observed nanoscale inhomogeneity of the SRO layer.

Therefore, we focus on the highly kinetic nature of PLD to understand the effect of the capping layer. During PLD, an incoming pulsed laser beam ablates the target and creates a plasma plume via laser-material interaction. The plume contains highly energetic species that will be transferred to the heated substrate.[50] Because the plume kinetics of PLD is mainly governed by the growth pressure,[51–53] its effect on the film heterostructure would be systematically tunable (**Figure 4**a,b). At high pressure, plume species experience many collisions and thus exhibit low kinetic energies. These species barely damage an already deposited film. On the other hand, at low pressure, plume species collide less, thus maintaining high velocities. Plume species bombard the already deposited film, creating serious modifications (red in Figure 4b). In our LAO/SRO double-layer films, a lower $P(O_2)_{LAO}$ creates Ru-deficient regions in the SRO layer, inducing an inhomogeneous (mixed) state. During LAO growth at low pressure, Ru atoms in SRO layer would be bombarded and eventually evaporate due to the high kinetic energy. As shown in the TOF-SIMS results (Figure 2e), it is unlikely that the Ru atoms migrate to the LAO capping layer because there is no significant Ru intensity in the capping layer. If the induced inhomogeneous phase has a positive AHE and a $T_C$ around 90 K, the experimental magnetic properties can be easily explained. The positive AHE in the inhomogeneous phase gives two-channel AHEs in SRO films, thus explaining the AHE humps (Figure 4c).

To verify our kinetics-based explanation, we performed additional control experiments using an $Ar/O_2$ gas mixture. With $P(O_2)_{LAO}$ fixed at 0.5 mTorr, we added Ar to increase the total pressure $P_{Total}$ inside the chamber. We varied $P_{Total}$ from 0.5 to 15.0 mTorr when growing LAO (10 u.c.)/SRO (5 u.c.) double-layer films. The $\rho_{AHE}$–$H$ curves are shown in Figure 4d–g. Using the two-component model described above, we fitted the $\rho_{AHE}$–$H$ curves with the negative (blue) and positive (red) components. As $P_{Total}$ decreases, the negative component decreases, and the positive component increases. The results of the control experiment are also plotted according to $P_{Total}$ (dashed black line in Figure 3k). The data are in reasonable agreement with those of the $P(O_2)_{LAO}$ control experiments, indicating that it is possible to tune the magnetotransport properties of $SrRuO_3$ ultrathin films by controlling the PLD kinetics.

The $M$–$T$ curves of the $P_{Total}$ control experiments are similar to those of the $P(O_2)_{LAO}$ control experiments (Figure S9, Supporting Information) in terms of pressure dependence. When an AHE hump is observed, the $M$–$T$ curves indicate the coexistence of the so-called 90 and 120 K phases. We also deposited the LAO layer at relatively high pressures, i.e., $P_{Total}$ = 50 and 100 mTorr (Figure S10, Supporting Information). The AHE of the SRO film is barely affected under such conditions. Therefore, our work suggests that bombardment by highly kinetic species in the plume explains the Ru deficiencies in the SRO layer induced during the deposition of capping layers which has light cations.

## 3. Conclusion and Outlook

We systematically investigated changes in the magnetic and two-channel AHEs of LAO/SRO double-layer films by using the high kinetic nature of PLD. We found that the growth pressure of the LAO capping layer is a crucial parameter for tuning the amount of nanoscale inhomogeneities. When the pressure is low, high-kinetic species transported during LAO deposition can modify the SRO layer. Our STEM and TOF-SIMS studies revealed inhomogeneous, nanoscale SRO regions of structural deformation and Ru deficiency, which can degrade the magnetic properties. The coexistence of inhomogeneous regions yields two-channel AHE signals, i.e., the hump anomalies.

Our work emphasizes the importance of in-depth exploration of high-kinetic PLD when creating oxide heterostructures. These exhibit intriguing physical properties, including multiple layers

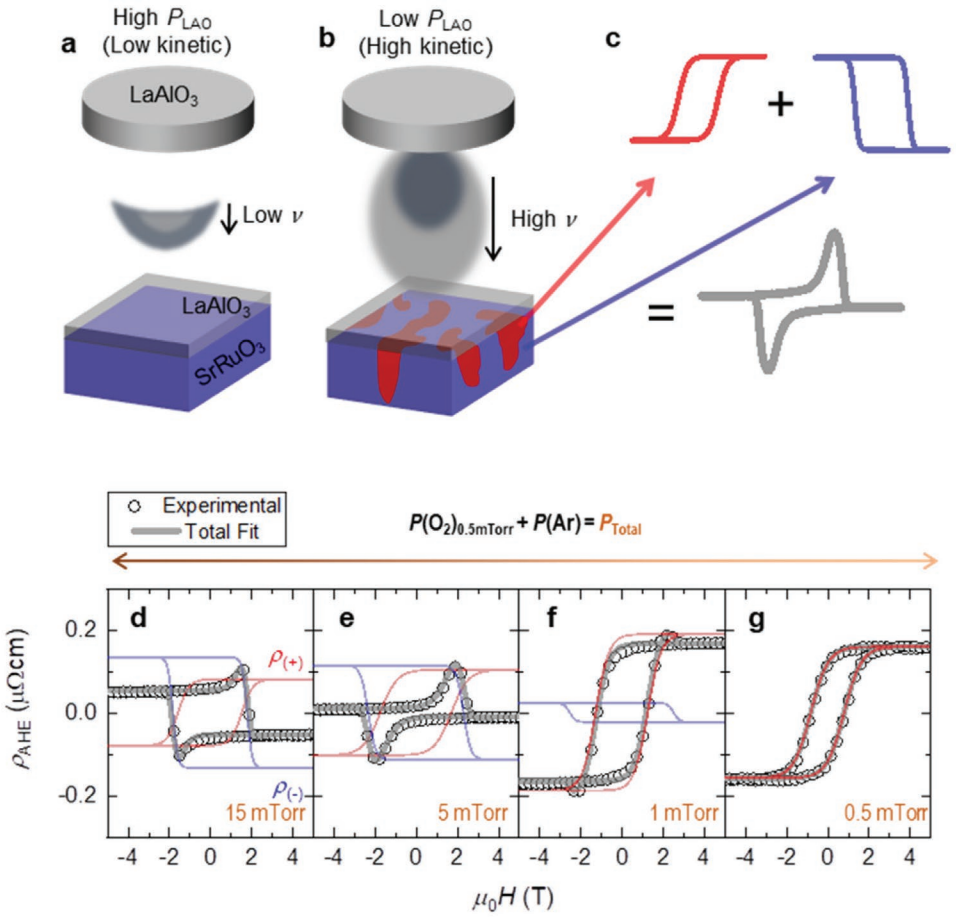


**Figure 4.** Schematics of PLD kinetics according to the background pressure, and a control experiment with total pressure variation during growth of the LAO capping layer. a) At high pressure, the kinetic energy of the evaporated plume is suppressed. b) At low pressure, the high kinetic energy of the evaporated plume induces SRO film inhomogeneities. The red regions in the SRO layer re inhomogeneous phases caused by the high kinetic energy of the adatoms. c) The red regions in the SRO film exhibit positive AHEs, as shown by the hump signals in the $\rho_{AHE}$–$H$ curve. d–g) $\rho_{AHE}$–$H$ curves derived by varying $P_{Total}$ from 15 to 0.5 mTorr. The $O_2$ partial pressure is fixed at 0.5 mTorr; only the Ar partial pressure is varied. The black open circles are the experimental curves and the red and blue curves the $\rho_{(-)}$- and $\rho_{(+)}$-fitting curves. The gray lines are the summations of the fitting curves. As $P_{Total}$ decreases, $\rho_{(+)}$ increases.

and superlattices. We found that highly kinetic bombardment generates nanoscale structural and compositional deformations, which significantly affect the macroscopic properties. Careful control of the kinetics allows for simple and effective tuning of the various properties of PLD-grown oxide heterostructures.

## 4. Experimental Section

*Sample Preparation*: STO(001) substrates (Crystec) were treated with buffered hydrofluoric acid and annealed at 1000 °C for 3 h in the ambient atmosphere. The treated substrates were $TiO_2$-terminated with atomically flat surfaces, showing step edges and terraces measured by AFM. SRO films were grown at 100 mTorr of oxygen pressure, and the temperature of the substrate was maintained as 700 °C. LAO films were grown at various pressures (0.5–100 mTorr with mixed pressure of oxygen and argon), and the growth temperature was 780 °C. For the growth, $SrRuO_3$ polycrystalline and $LaAlO_3$(001) substrate (Shinkosha) were used as targets. The targets were ablated by a KrF excimer laser (≈248 nm, Coherent). The laser fluence was 2 and 1 J $cm^{-2}$ for SRO and LAO films, respectively.

*Transport and Magnetization Measurement*: 50 × 50 $\mu m^2$ sized Hall bars were fabricated on the films with ultraviolet photolithography and Ar ion milling system. AZ5214E was used as a photoresist. 20 nm of Au was deposited as an electrode with electron beam evaporation. The transverse transport data were measured by Physical Properties Measurement System (PPMS, Quantum Design). Temperature dependence magnetization was measured in vibrating sample magnetometry (VSM) mode using a SQUID magnetometer, by a Magnetic Properties Measurement System (MPMS, Quantum Design). They were measured during cooling with 100 Oe of out-of-plane applied field. Straws were used as sample holders. The backside of the substrates was polished with sandpaper to remove the possible magnetic signal from the Pt paste used for the growth.

*Scanning Transmission Electron Microscopy Measurements*: An electron transparent STEM specimen was prepared by focused ion beam milling (Helios 650 FIB, FEI) and further thinned by focused Ar-ion milling (NanoMill 1040, Fischione). Cross-sectional STEM images were acquired at room temperature using a spherical aberration-corrected STEM (Themis Z, Thermo Fisher Scientific Inc.) equipped with a high-brightness Schottky-field emission gun operated with a 300kV electron acceleration voltage. The semiconvergence angle of the electron probe was 17.9 mrad. The collection semi-angle for ABF was 10–21 mrad.

*Time-of-Flight Secondary Ion Mass Spectrometry*: Each sample was etched with Cs ion accelerated by 0.5 keV of energy at the base pressure of 3.8 × $10^{-9}$ Torr during the measurement. The etched area was

$500 \times 500\ \mu m^2$ and the analyzed area was $100 \times 100\ \mu m^2$. The emitted cations (secondary ion) from the etching process were measured by the mass analyzer (TOF.SIMS-5, IONTOF). Sputtering time is proportional to the probing depth, thus the TOF-SIMS plot gives depth-profile information of the sample stoichiometry.

*Fitting for $\rho_{AHE}$–H and M–T Curves*: $\rho_{AHE}$ is the anomalous Hall resistivity where the linear term of the ordinary Hall effect is subtracted from the total transverse Hall resistivity (Figure S4, Supporting Information). To fit the AHE curves, hyperbolic tangent function, $\rho_{AHE}(H) = a \cdot \tanh(b \cdot (H - H_C))$ was used. Fitting parameters were saturated amplitude ($a$), broadening ($b$), and coercive field ($H_C$). To fit the *M–T* curves, empirical magnetization function, $M(T) = M(0) \cdot (1 - (T/T_C)^{\alpha})^{\beta}$ was used. Fitting parameters were $T_C$, saturation amplitude ($M(0)$), and exponents ($\alpha$, $\beta$). The least-square approximation was conducted using the MATLAB software (MathWorks). The ratio of 90 K phase from the *M–T* curves was derived from magnetization at 10 K of the two phases.

*Structure and Surface Characterizations*: XRD (D8 Discover; Bruker) with a Cu K$\alpha$-1 source ($\lambda$ = 1.5406 Å) and AFM (Cypher; Asylum Research) were used. XRD was also performed by synchrotron-based XRD using the Huber six-circle diffractometers at Sector 3A of the Pohang Light Source (South Korea).

## Supporting Information

Supporting Information is available from the Wiley Online Library or from the author.

## Acknowledgements

E.K.K. and H.G.L. contributed equally to this work. All the authors want to thank the major support from the Research Center Program of IBS (Institute for Basic Science) in Korea (IBS-R009-D1). S.L., J.M., and M.K. acknowledge the financial support from the Korean government through National Research Foundation (2017R1A2B3011629). Cs-corrected STEM works were supported by the Research Institute of Advanced Materials (RIAM) in Seoul National University. S.B.C. was supported by the National Research Foundation of Korea (NRF) grants funded by the Korea government (MSIT) (2020R1A2C1007554) and the Ministry of Education (2018R1A6A1A06024977). PPMS and TOF-SIMS measurements were supported by the National Center for Inter-University Research Facilities (NCIFR) at Seoul National University in Korea. Experiments at PLS-II 3A beamline were supported in part by MSIT and POSTECH. The authors also acknowledge discussion from Dr. Wei Peng, Dr. Byungmin Sohn, Dr. Gideok Kim, Dr. Jeong Rae Kim, Dr. Changjae Roh, and Subin Kim.

## Conflict of Interest

The authors declare no conflict of interest.

## Data Availability Statement

The data that support the findings of this study are available in the supplementary material of this article.

## Keywords

anomalous Hall effect, epitaxial thin films, nanoscale inhomogeneity of perovskite $SrRuO_3$, pulsed laser deposition

Received: August 4, 2021
Revised: October 1, 2021
Published online: November 11, 2021

[1] A. Ohtomo, H. Y. Hwang, *Nature* **2004**, *427*, 423.
[2] D. G. Schlom, L.-Q. Chen, X. Pan, A. Schmehl, M. A. Zurbuchen, *J. Am. Ceram. Soc.* **2008**, *91*, 2429.
[3] J. M. Rondinelli, S. J. May, J. W. Freeland, *MRS Bull.* **2012**, *37*, 261.
[4] S. Thiel, G. Hammerl, A. Schmehl, C. W. Schneider, J. Mannhart, *Science* **2006**, *313*, 1942.
[5] D. G. Schlom, L.-Q. Chen, C. J. Fennie, V. Gopalan, D. A. Muller, X. Pan, R. Ramesh, R. Uecker, *MRS Bull.* **2014**, *39*, 118.
[6] J. He, A. Borisevich, S. V. Kalinin, S. J. Pennycook, S. T. Pantelides, *Phys. Rev. Lett.* **2010**, *105*, 227203.
[7] N. Reyren, S. Thiel, A. D. Caviglia, L. F. Kourkoutis, G. Hammerl, C. Richter, C. W. Schneider, T. Kopp, A.-S. Rüetschi, D. Jaccard, M. Gabay, D. A. Muller, J.-M. Triscone, J. Mannhard, *Science* **2007**, *317*, 1196.
[8] G. Koster, L. Klein, W. Siemons, G. Rijnders, J. S. Dodge, C.-B. Eom, D. H. A. Blank, M. R. Beasley, *Rev. Mod. Phys.* **2012**, *84*, 253.
[9] P. B. Allen, H. Berger, O. Chauvet, L. Forro, T. Jarlborg, A. Junod, B. Revaz, G. Santi, *Phys. Rev. B* **1996**, *53*, 4393.
[10] C. B. Eom, R. B. Van Dover, J. M. Phillips, D. J. Werder, J. H. Marshall, C. H. Chen, R. J. Cava, R. M. Fleming, D. K. Fork, *Appl. Phys. Lett.* **1993**, *63*, 2570.
[11] S. G. Jeong, H. Kim, S. J. Hong, D. Suh, W. S. Choi, *ACS Appl. Nano Mater.* **2021**, *4*, 2160.
[12] J. Matsuno, N. Ogawa, K. Yasuda, F. Kagawa, W. Koshibae, N. Nagaosa, Y. Tokura, M. Kawasaki, *Sci. Adv.* **2016**, *2*, e1600304.
[13] Y. Ohuchi, J. Matsuno, N. Ogawa, Y. Kozuka, M. Uchida, Y. Tokura, M. Kawasaki, *Nat. Commun.* **2018**, *9*, 213.
[14] Z. Fang, N. Nagaosa, K. S. Takahashi, A. Asamitsu, R. Mathieu, T. Ogasawara, H. Yamada, M. Kawasaki, Y. Tokura, K. Terakura, *Science* **2003**, *302*, 92.
[15] N. Nagaosa, J. Sinova, S. Onoda, A. H. MacDonald, N. P. Ong, *Rev. Mod. Phys.* **2010**, *82*, 1539.
[16] K. S. Takahashi, H. Ishizuka, T. Murata, Q. Y. Wang, Y. Tokura, N. Nagaosa, M. Kawasaki, *Sci. Adv.* **2018**, *4*, eaar7880.
[17] L. Wang, Q. Feng, Y. Kim, R. Kim, K. H. Lee, S. D. Pollard, Y. J. Shin, H. Zhou, W. Peng, D. Lee, W. Meng, H. Yang, J. H. Han, M. Kim, Q. Lu, T. W. Noh, *Nat. Mater.* **2018**, *17*, 1087.
[18] R. Mathieu, A. Asamitsu, K. Takahashi, H. Yamada, M. Kawasaki, Z. Fang, N. Nagaosa, Y. Tokura, *J. Magn. Magn. Mater.* **2004**, *272*, E785.
[19] L. Klein, J. S. Dodge, C. H. Ahn, G. J. Snyder, T. H. Geballe, M. R. Beasley, A. Kapitulnik, *Phys. Rev. Lett.* **1996**, *77*, 2774.
[20] Y. Kats, I. Genish, L. Klein, J. W. Reiner, M. R. Beasley, *Phys. Rev. B* **2004**, *70*, 180407.
[21] B. Sohn, E. Lee, W. Kyung, M. Kim, H. Ryu, J. S. Oh, D. Kim, J. K. Jung, B. Kim, M. Han, T. W. Noh, B. J. Yang, C. Kim, *Nature Mater.* **2021**, https://doi.org/10.1038/s41563-021-01101-4.
[22] M. Ziese, L. Jin, I. Lindfors-Vrejoiu, *J. Phys. Mater.* **2019**, *2*, 034008.
[23] H. G. Lee, L. Wang, L. Si, X. He, D. G. Porter, J. R. Kim, E. K. Ko, J. Kim, S. M. Park, B. Kim, A. T. S. Wee, A. Bombardi, Z. Zhong, T. W. Noh, *Adv. Mater.* **2019**, 1905815.
[24] E. K. Ko, J. Mun, H. G. Lee, J. Kim, J. Song, S. H. Chang, T. H. Kim, S. B. Chung, M. Kim, L. Wang, T. W. Noh, *Adv. Funct. Mater.* **2020**, *30*, 2001486.
[25] Y. Gu, C. Song, Q. Zhang, F. Li, H. Tan, K. Xu, J. Li, M. S. Saleem, M. U. Fayaz, J. Peng, F. Hu, L. Gu, W. Liu, Z. Zhang, F. Pan, *ACS Mater. Interfaces* **2020**, *12*, 6707.
[26] Y. Gu, Y. Wei, K. Xu, H. Zhang, F. Wang, F. Li, M. S. Saleem, C. Chang, J. Sun, C. Song, J. Feng, X. Zhong, W. Liu, Z. Zhang, J. Zhu, F. Pan, *J. Phys. D: Appl. Phys.* **2019**, *52*, 404001.
[27] D. Kan, T. Moriyama, K. Kobayashi, Y. Shimakawa, *Phys. Rev. B* **2018**, *98*, 180408.
[28] D. Kan, T. Moriyama, Y. Shimakawa, *Phys. Rev. B* **2020**, *101*, 014448.
[29] D. J. Groenendijk, C. Autieri, T. C. van Thiel, W. Brzezicki, N. Gauquelin, P. Barone, K. H. W. van den Bos, S. van Aert,

J. Verbeeck, A. Filippetti, S. Picozzi, M. Cuoco, A. D. Caviglia, *Phys. Rev. Res.* **2020**, *2*, 023404.
[30] L. Wang, Q. Feng, H. G. Lee, E. K. Ko, Q. Lu, T. W. Noh, *Nano Lett.* **2020**, *20*, 2468.
[31] G. Kimbell, P. M. Sass, B. Woltjes, E. K. Ko, T. W. Noh, W. Wu, J. W. A. Robinson, *Phys. Rev. Mater.* **2020**, *4*, 054414.
[32] L. Miao, N. J. Schreiber, H. P. Nair, B. H. Goodge, S. Jiang, J. P. Ruf, Y. Lee, M. Fu, B. Tsang, Y. Li, C. Zeledon, J. Shan, K. F. Mak, L. F. Kourkoutis, D. G. Schlom, K. M. Shen, *Phys. Rev. B* **2020**, *102*, 064406.
[33] G. Kim, K. Son, Y. E. Suyolcu, L. Miao, N. J. Schreiber, H. P. Nair, D. Putzky, M. Minola, G. Christiani, P. A. Van Aken, K. M. Shen, D. G. Schlom, G. Logvenov, B. Keimer, *Phys. Rev. Mater.* **2020**, *4*, 104410.
[34] L. Wysocki, L. Yang, F. Gunkel, R. Dittmann, P. H. M. Van Loosdrecht, I. Lindfors-Vrejoiu, *Phys. Rev. Mater.* **2020**, *4*, 054402.
[35] L. Yang, L. Wysocki, J. Schöpf, L. Jin, A. Kovács, F. Gunkel, R. Dittmann, P. H. M. Van Loosdrecht, I. Lindfors-Vrejoiu, *Phys. Rev. Mater.* **2021**, *5*, 014403.
[36] E. Skoropata, A. R. Mazza, A. Herklotz, J. M. Ok, G. Eres, M. Brahlek, T. R. Charlton, H. N. Lee, T. Z. Ward, *Phys. Rev. B* **2021**, *103*, 085121.
[37] B. Sohn, B. Kim, S. Y. Park, H. Y. Choi, J. Y. Moon, T. Choi, Y. J. Choi, T. W. Noh, H. Zhou, S. H. Chang, J. H. Han, C. Kim, *Phys. Rev. Reserach* **2021**, *3*, 023232.
[38] Q. Qin, L. Liu, W. Lin, X. Shu, Q. Xie, Z. Lim, C. Li, S. He, G. M. Chow, J. Chen, *Adv. Mater.* **2019**, *31*, 1807008.
[39] D. Liang, J. P. DeGrave, M. J. Stolt, Y. Tokura, S. Jin, *Nat. Commun.* **2015**, *6*, 8217.
[40] M. Golalikhani, Q. Y. Lei, G. Chen, J. E. Spanier, H. Ghassemi, C. L. Johnson, M. L. Taheri, X. X. Xi, *J. Appl. Phys.* **2013**, *114*, 027008.
[41] M. Bohra, C. P. Wu, H. J. Yeh, Y. H. Cheng, C. C. Peng, H. Chou, *J. Appl. Phys.* **2011**, *109*, 07D728.
[42] Y. K. Wakabayashi, S. Kaneta-Takada, Y. Krockenberger, K. Takiguchi, S. Ohya, M. Tanaka, Y. Taniyasu, H. Yamamoto, *Am. Inst. Phys. Adv.* **2021**, *11*, 035226.
[43] H. Kronmüller, *Phys. Status Solidi* **1987**, *144*, 385.
[44] D. Givord, M. F. Rossignol, D. W. Taylor, *J. Phys. IV* **1992**, *2*, C3 95.
[45] H. N. Lee, H. M. Christen, M. F. Chisholm, C. M. Rouleau, D. H. Lowndes, *Appl. Phys. Lett.* **2004**, *84*, 4107.
[46] J. Shin, A. Y. Borisevich, V. Meunier, J. Zhou, E. W. Plummer, S. V. Kalinin, A. P. Baddorf, *ACS Nano* **2010**, *4*, 4190.
[47] H. L. Hu, L. Ao, A. Pham, D. Wang, Y. Wang, Z. Chen, C. Kong, T. T. Tan, X. Zu, S. Li, *Adv. Mater. Interfaces* **2016**, *3*, 1600547.
[48] E. J. Guo, Y. Liu, C. Sohn, R. D. Desautels, A. Herklotz, Z. Liao, J. Nichols, J. W. Freeland, M. R. Fitzsimmons, H. N. Lee, *Adv. Mater.* **2018**, *30*, 1705904.
[49] T. T. Mayeshiba, D. D. Morgan, *Solid State Ionics* **2016**, *296*, 71.
[50] R. Eason, *Pulsed Laser Deposition of Thin Films*, Wiley-Interscience **2006**.
[51] J. N. Leboeuf, K. R. Chen, J. M. Donato, D. B. Geohegan, C. L. Liu, A. A. Puretzky, R. F. Wood, *Phys. Plasmas* **1996**, *3*, 2203.
[52] S. Lafane, T. Kerdja, S. Abdelli-Messaci, Y. Khereddine, M. Kechouane, O. Nemraoui, *Appl. Phys. A: Mater. Sci. Process.* **2013**, *112*, 159.
[53] A. Ojeda-G-P, C. W. Schneider, M. Döbeli, T. Lippert, A. Wokaun, *J. Appl. Phys.* **2017**, *121*, 135306.